J Mater Sci

Ceramics

Palladium exsolution and dissolution with lanthanum ferrite perovskite oxides

Seyed Morteza Taghavi Kouzehkanan[1], Jong-Eun Hong[2], and Tae-Sik Oh[1,*]

[1] *Department of Chemical Engineering, Auburn University, Auburn, AL 36849, USA*
[2] *High Temperature Energy Conversion Laboratory, Korea Institute of Energy Research, 152 Gajeong-ro, Yuseong-gu, Daejeon 34129, Republic of Korea*

Received: 7 November 2022
Accepted: 23 February 2023

ABSTRACT

Metal exsolution catalyst has gained interest from catalysis researchers due to the unique properties such as coarsening resistance and coking resistance. We closely inspected X-ray diffraction patterns from thermally treated powders to understand the palladium exsolution/dissolution with an ABO_3 perovskite oxide, lanthanum ferrite (LFO). A-site full composition was chosen with only Fe and Pd on the B-sites to test the reversibility. We added Fe_2O_3 to the Pd-doped LFO to check its impact on reversibility. The addition of Fe_2O_3 did not facilitate Pd exsolution or alter the reversibility of the Pd exsolution/dissolution. A complete dissolution of exsolved Pd into the Fe matrix was observed at 800 °C, suggesting Pd exsolution from LFO is a surface phenomenon. The Pd dissolution into A-site full lanthanum ferrite in the air showed the emergence of Fe_2O_3. However, this Fe_2O_3 formation can be seen only in a certain temperature range.

Introduction

Metal exsolution from oxide matrix has gained interest from heterogeneous catalysis researchers. In this scheme, the catalyst system starts from a single phase oxide with easily reducible metal dissolved within the oxide lattice. Under the reducing condition, the easily reducible cation turns to metal, decorating the oxide surface with well-dispersed nanoparticles. The catalyst fabrication route has provided metal nanoparticle catalysts of unique properties. The simultaneous sintering resistance and coking resistance of the exsolved nickel catalyst have been demonstrated [1]. The possibility of electrochemical control is also attractive [2].

The first reported metal exsolution, as opposed to dissolution, catalyst system was $LaFe_{0.57}Co_{0.38}Pd_{0.05}O_3$, where palladium particles emerged under reduction [3]. The exsolved metal can be re-dissolved into the oxide lattice as cation by oxidation, and regeneration of Pd particles takes place by reducing

Handling Editor: David Cann.

Address correspondence to E-mail: taesik.oh@auburn.edu

https://doi.org/10.1007/s10853-023-08346-1

Published online: 11 March 2023

the oxide again. This reversibility, often described as "intelligent" or "regenerative," of the catalyst system has been proved useful for automotive emission control. Lanthanum ferrite was later applied to support Re–Ni–Fe alloy exsolution particles for methane dry reforming [4]. Pd-doped lanthanum ferrite was investigated for natural gas vehicle three-way catalysis utilizing the exsolution of Pd [5, 6].

The metal exsolution concept has been successfully applied to electrochemical cells. $La_{0.8}Sr_{0.2}Cr_{0.82}Ru_{0.18}O_3$ was the first solid oxide fuel cell anode that utilized exsolved ruthenium nanoparticle for hydrogen electrooxidation [7]. The regeneration of the metal particles in the solid oxide electrochemical cells for either electrooxidation or electrolysis has been demonstrated with Pd [8, 9], Fe [10], Ni [11], and Co–Fe alloy [12].

The history of metal exsolution catalysts is relatively short; however, in the ceramics field the same partial decomposition of the oxide was studied long ago. The terminology used to describe the metal exsolution was "internal reduction" in the old literature [13–18]. The "internal reduction" was a phenomenon that was studied after "internal oxidation" was observed in alloys of Cu–Pd and Cu–Pt [19]. As the name suggests, in "internal oxidation," copper oxide forms within the noble metal matrix. This oxidation of copper inside of metal matrix is the opposite of the metal exsolution, while both cases involve solid-state phase separation of the initial single-phase material. The oxide researchers did not look into the utilization of the metal particles from the oxide partial decomposition for catalysis.

Recently, there have been efforts to control the metal exsolution by adding a second phase. This strategy is called "topotactic exchange" where a metal is going into the host lattice inducing exsolution of another metal [20]. For a double perovskite $PrBaMn_{1.7}Co_{0.3}O_{5+\delta}$, iron is added to the oxide surface during the reduction. Fe entered the host lattice while Co came out of the lattice to form Co–Fe alloy on the surface. The amount of iron went into the lattice was proportional to the amount of exsolved cobalt [21].

In this study, we went back to the original ABO_3 perovskite lattice of lanthanum ferrite. We fabricated the perovskite without cobalt to simplify the material system and chose palladium as a representative exsolution metal. With this simplest oxide system that can promote palladium exsolution, we investigated the reversibility of the palladium exsolution/dissolution and the impact of the Fe_2O_3 addition. The commonly adopted A-site deficient composition was not used for the lanthanum ferrite since A-site deficiency will not result in a reversible exsolution/dissolution system.

Experimental

Synthesis of Pd-doped lanthanum ferrite

Bulk $LaFe_{0.95}Pd_{0.05}O_3$ and $LaFe_{0.9}Pd_{0.1}O_3$ powders were prepared by sol–gel process using $La(NO_3)\text{-}6H_2O$ (Alfa Aesar, 99%), $Fe(NO_3)_3{\cdot}9H_2O$ (Alfa Aesar, 98.5%), $Pd(NO_3)_2{\cdot}2H_2O$ (Sigma-Aldrich), citric acid (Fischer Scientific), and de-ionized water. The desired stoichiometric amount of nitrates was dissolved in de-ionized water under magnetic stirring. To the nitrate solution, citric acid was added as a chelating agent to promote the ABO_3 perovskite phase formation. The molar ratio of all metal cations to citric acid was set to be 1. The precursor solution was heated to 350 °C on a hot plate to achieve the gel. The gel was then calcined in ambient air for 4 h to achieve the perovskite phase. Undoped $LaFeO_3$ and $La_{0.95}FeO_3$ were also fabricated using the same procedure with calcination temperature at 900 °C.

Ex situ Pd exsolution and dissolution study

X-ray diffraction (XRD) patterns were collected to identify solid phases. For high-temperature Pd exsolution, hydrogen was used to reduce the perovskite oxide. In most of the reduction tests, the hydrogen gas was bubbled through a water reservoir held at room temperature leading to 3 vol% water vapor in the balance hydrogen. When dry hydrogen was used, the gas directly came from the tank without humidification. Fe_2O_3 powder (Alfa Aesar) was added to the perovskite powder sample at 1:1 weight ratio with physical mixing to see the impact of its presence on the Pd exsolution. Reaction temperatures ranged from 500 to 800 °C with 100 °C interval. Some of the reduced powder samples were re-oxidized in air to check the reversibility of the Pd exsolution/dissolution.

Results and discussion

Lanthanum ferrite perovskite formation

Figure 1 shows the X-ray diffraction patterns of the as-synthesized Pd-doped lanthanum ferrites (LFO-PdX, X = 5 or 10 at%). 5 at% doped ferrite did not show the sign of La_2PdO_4 formation, whereas higher doping level of the palladium (10 at%) led to formation of La_2PdO_4. Figure 1a shows the X-ray diffraction pattern of LFO-Pd5 calcined at 900 °C in air. The La_2PdO_4 impurity phase persisted for all samples of 10 at% doping as shown in Fig. 1b; therefore, we chose LFO-Pd10 sample that is calcined at 850 °C for further study since it had the weakest La_2PdO_4 diffraction peak among the samples from four different calcination temperatures. For LFO-Pd5, 900 °C calcined sample was used for further study.

Impact of the humidity in the reducing hydrogen gas

The humidity in the hydrogen gas can change the chemical composition of the exsolved metal particles. Figure 2 shows comparison of the X-ray diffraction patterns of LFO-Pd5 samples reduced at 800 °C for 4 h by dry hydrogen and wet hydrogen. Exsolved metal peaks are detected in both cases. For the wet hydrogen sample, we can see the FCC (111) peak and (200) peak, while only FCC (111) peak is clearly observed for dry hydrogen sample. Since Pd has larger lattice parameter than Fe in the face-centered cubic structure, the metal peak positions suggest that Pd-rich alloy particles emerge when the reducing gas is humid. The oxygen partial pressure will be lower in the dry hydrogen, and this strong reduction

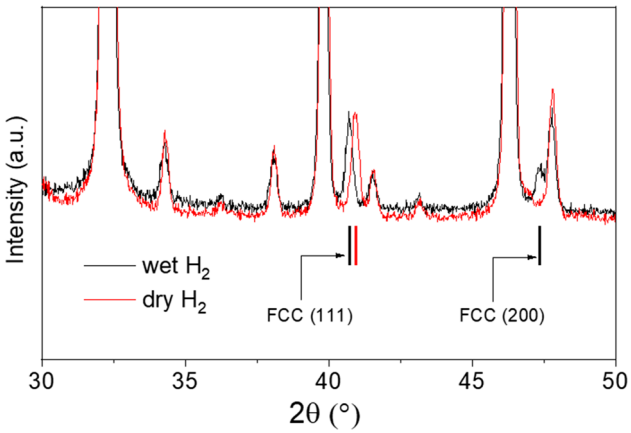

Figure 2 Comparison of the X-ray diffraction patterns after LFO-Pd5 reduction. Dry hydrogen induced exsolution of Pd-Fe alloy particles.

driving force can pull metallic iron out of the oxide lattice along with metallic palladium.

Without palladium, iron exsolution is not possible under the same reducing condition even from an A-site deficient composition, $La_{0.95}FeO_3$. Figure 3 shows no exsolution of iron, suggesting that emerging Pd particles provide active surface for iron incorporation. Fe incorporation in the Pd particles can be interesting for heterogeneous catalyst applications; however, we focused on the wet hydrogen samples in this study.

Reversibility

The reversibility of the palladium exsolution/dissolution process was checked by re-oxidizing reduced samples. Figure 4 illustrates the phase content evolution of LFO-Pd5 and LFO-Pd10. The reduction was conducted for 4 h under wet hydrogen at 800 °C. The same temperature and duration applied to re-

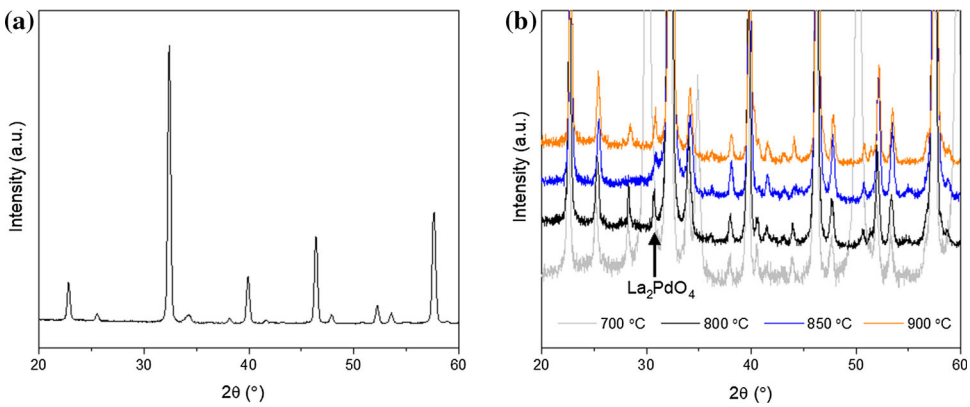

Figure 1 **a** An X-ray diffraction pattern from LFO-Pd5 ($LaFe_{0.95}Pd_{0.05}O_3$) after 900 °C calcination in air for 4 h. **b** X-ray diffraction patterns from LFO-Pd10 ($LaFe_{0.9}Pd_{0.1}O_3$) synthesized at different temperatures.

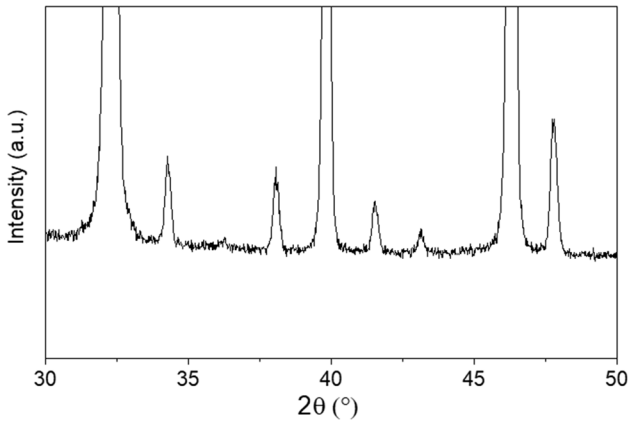

Figure 3 An XRD pattern from A-site deficient $La_{0.95}FeO_3$ after 800 °C, 4 h reduction by dry hydrogen.

oxidization step under ambient air. For both doping levels, the palladium exsolution and dissolution is largely reversible. For LFO-Pd10, palladium exsolution accompanied La_2O_3 formation at 800 °C, which is evidenced by $La(OH)_3$ diffraction peaks in the red-outlined box. The La_2O_3 particles reacted with adventitious humidity to form $La(OH)_3$ at room temperature. Even with this hydroxide formation, the re-oxidation successfully re-incorporated lanthanum into the perovskite matrix, as expected. It is noted that the initial La_2PdO_4 phase in LFO-Pd10 disappeared after the reduction–oxidation cycle.

The same cycling test was conducted for powder mixtures of Pd-doped LFO and Fe_2O_3 (1:1 weight ratio). Figure 5 shows the phase content evolution. As expected, the high-temperature reduction gave rise to metallic iron formation. The 800 °C reduction resulted in no metal diffraction peak at 40.5° 2θ angle for LFO-Pd5. This lack of palladium metal-related peak means that the exsolved palladium particles got fully dissolved into the iron matrix. For LFO−Pd10 + Fe_2O_3 mixture, the dissolution of palladium into the surrounding metallic iron is not as obvious. The amount of exsolved palladium should be higher for the LFO-Pd10, so longer reduction time may be needed to have all palladium dissolved into the iron matrix.

Impact of Fe_2O_3 second phase during reduction

We investigated how the presence of the Fe_2O_3 will affect the palladium exsolution behavior. For LFO-Pd5 sample, Fe_2O_3 addition did not change the post-reduction XRD patterns after 4 h reduction under wet hydrogen at 500, 600, and 700 °C (Fig. 6). After 500 °C reduction, the diffraction patterns already showed metal exsolution. It has been reported that the palladium exsolution starts at 200 °C from the lanthanum ferrite lattice [22]. At 800 °C, the exsolved palladium clearly dissolved into iron matrix, showing no diffraction peak between 40 and 41°.

For LFO-Pd10, a similar trend has been observed (Fig. 7). The XRD patterns showed difference only at 800 °C. The dissolution of exsolved palladium into iron is not as pronounced as in LFO-Pd5; however, the difference can still be seen in the 2θ range of 40–42°.

The XRD results show that the interaction between the Fe_2O_3 and Pd-doped lanthanum ferrite is weak in general. The addition of Fe_2O_3 does not seem to facilitate Pd exsolution. The iron matrix made the metallic Pd peak from LFO-Pd5 disappear. The

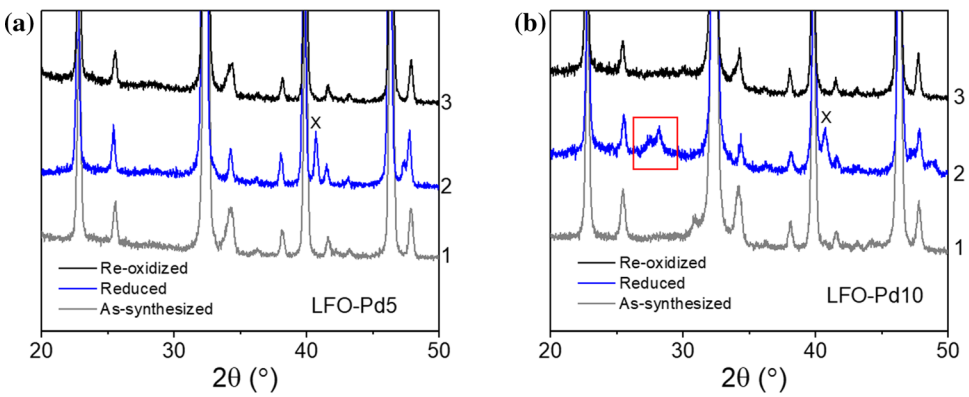

Figure 4 **a** Reversible phase evolution of LFO-Pd5 during reduction–oxidation cycle. **b** Reversible phase evolution of LFO-Pd10. Reduction condition: wet H_2, 800 °C, 4 h. Oxidation condition: ambient air, 800 °C, 4 h. The primary peak of the exsolved metal is marked with an "X" sign. The numbers next to the traces denote the data collection sequence.

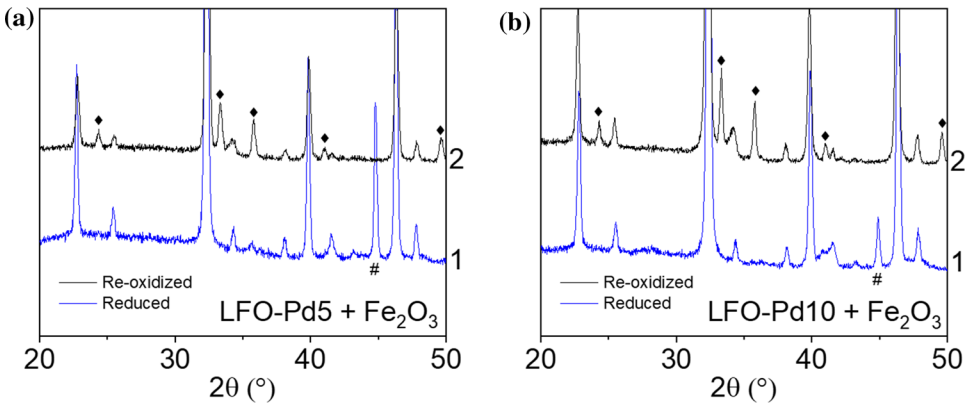

Figure 5 **a** Reversible phase evolution of LFO-Pd5 + Fe_2O_3. **b** Reversible phase evolution of LFO-Pd10 + Fe_2O_3. Reduction condition: wet H_2, 800 °C, 4 h. Oxidation condition: ambient air, 800 °C, 4 h. Re-oxidation brought Fe_2O_3 peaks (marked with "◆"), while the metallic iron peak (marked with "#") disappeared.

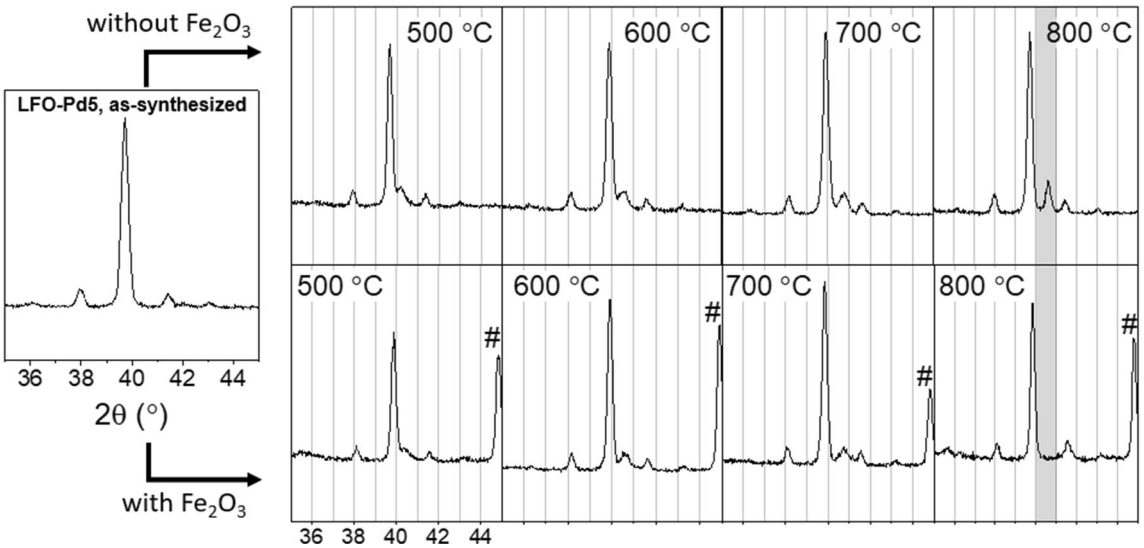

Figure 6 Comparison of the X-ray diffraction patterns for LFO-Pd5 reduction. The addition of Fe_2O_3 made difference only at 800 °C. "#" marks a metallic iron peak.

complete dissolution of the exsolved Pd into surrounding iron suggests that we do not have Pd nuclei within the perovskite matrix. The Pd nucleation sites are on the ferrite surface rather than within the subsurface region. This behavior differs from the nickel exsolution out of the lanthanum titanates [23].

Palladium dissolution into A-site full lanthanum ferrite

In addition to the Pd-doped LFO phase evolution study, we reacted undoped A-site full lanthanum ferrite with $Pd(NO_3)_2{\cdot}2H_2O$. The palladium source was dissolved in water and impregnated to the ferrite powder for uniform loading on the oxide surface [24]. The nominal Pd-to-Fe atomic ratio was 4:96 in the impregnated powder. Figure 8 compares the XRD patterns of the same composition, $LaFeO_3$ (900 °C calcination) + Pd source, after separately annealed in air at two different temperatures: 1100 and 1500 °C. After 4-h annealing at 1100 °C, there was a small peak of Fe_2O_3 marked with an arrow. This (104) reflection is the strongest peak from bulk Fe_2O_3 powder. The incorporation of the Pd on the Fe site forced Fe to come out of the perovskite lattice forming Fe_2O_3 secondary phase. This Fe_2O_3 peak is not clear for the 1500 °C sample. The Fe_2O_3 particles became re-incorporated into the perovskite lattice by the high-temperature annealing.

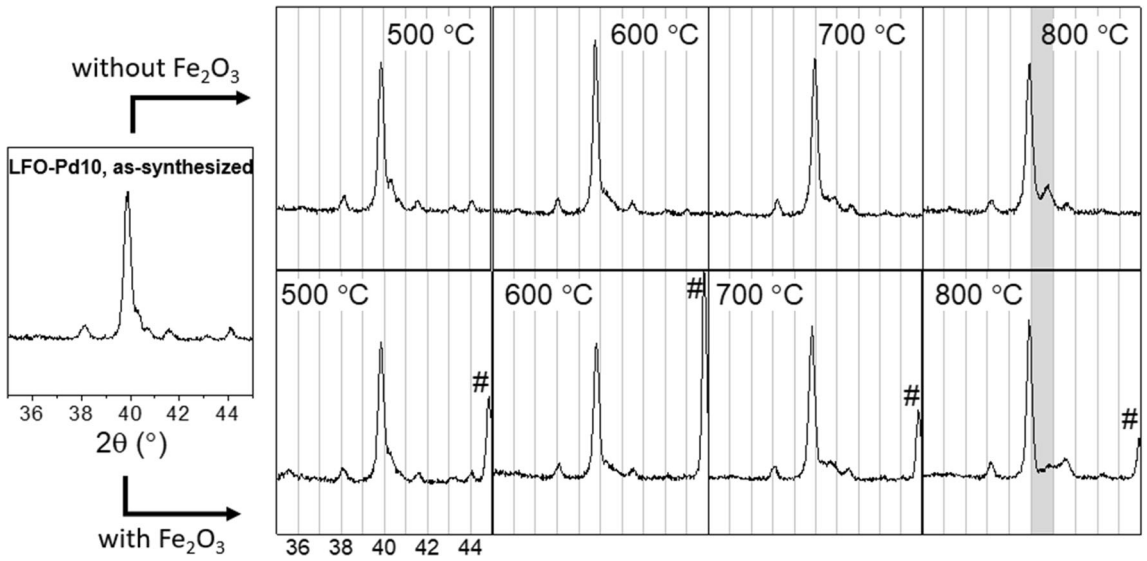

Figure 7 Comparison of the X-ray diffraction patterns for LFO-Pd10 reduction. The addition of Fe_2O_3 made difference only at 800 °C. "#" marks a metallic iron peak.

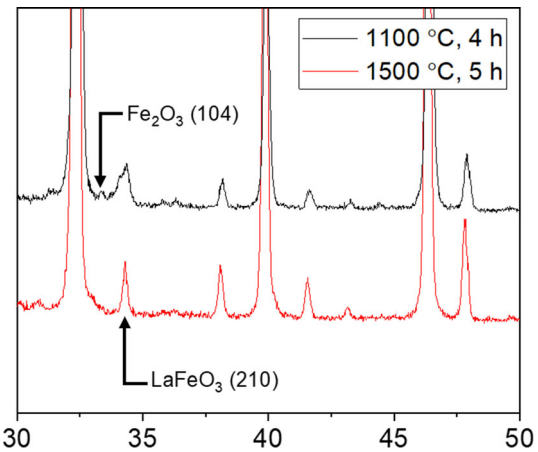

Figure 8 Pd dissolution behavior into LFO lattice monitored by XRD.

In addition, the perovskite (210) diffraction peak from the 1100 °C sample looks broader, especially on the smaller angle side, than the one from 1500 °C sample. We interpret that the skewed peak shape comes from superposition of PdO (101) peak and perovskite (210) peak. A comparison between the experimental profile and computed one is shown in the supporting information (Figure S1). A small amount of PdO was still remaining out of the perovskite lattice after 1100 °C annealing. This small amount PdO apparently dissolved into the perovskite lattice after 1500 °C heat treatment leading to the sharp and symmetric perovskite (210) peak (red scan in Fig. 8). The small amount of the PdO would exist as Pd under reducing condition. Figure 9 shows room temperature XRD pattern of $PdCl_2$-alumina powder mixture ($PdCl_2/Al_2O_3$ = 1:4 by weight) after 900 °C 5-h annealing in air. Metallic Pd peaks were still visible after cooling in air since Pd is more stable than PdO in ambient air at 900 °C. PdO formed during the air cooling, but the oxidation was not complete.

Knowing the close diffraction peak positions of PdO (101) and LFO (210), we closely re-examined as-synthesized LFO-Pd5 (900 °C calcination) and LFO-Pd10 (850 °C calcination). We indeed had the superposition of PdO (101) peak and LFO (210) peak for these as-synthesized samples (Fig. 4). Even though

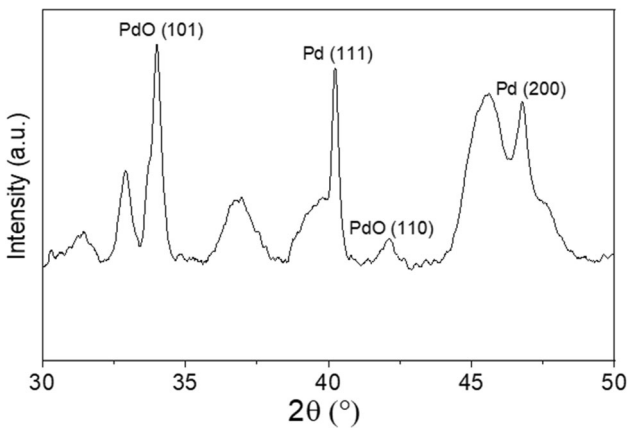

Figure 9 Remaining Pd diffraction peaks from air-annealed $PdCl_2$-alumina composite.

some PdO particles were outside the perovskite lattice, the as-synthesized LFO lattice had Pd ions on its B-sites, as evidenced by the $La(OH)_3$ diffraction peaks after reduction. If the LFO perovskite lattice had no Pd within, we would not have partial decomposition of the perovskite lattice under reducing condition.

Conclusion

Pd-doped lanthanum ferrites were fabricated via the sol–gel route to investigate the Pd exsolution/dissolution behavior. For both 5% doped and 10% doped LFO from sol–gel synthesis, a small amount of PdO was present. Its presence, however, did not have a distinguishable impact on Pd exsolution/dissolution behavior.

The humidity in the reducing hydrogen gas can change the composition of the exsolved metal. With dry hydrogen, we have iron dissolved in palladium for the emerging metallic phase. With wet hydrogen, the metallic phase is mostly just palladium. Dry hydrogen did not make metallic iron particles come out, even from an A-site deficiency composition of $La_{0.95}FeO_3$. The exsolved palladium surface provides easily accessible attachment sites for iron atoms.

The addition of Fe_2O_3 did not facilitate Pd exsolution. The reversibility of the Pd exsolution/dissolution remained the same. Up to the wet hydrogen reduction temperature of 700 °C, there is no difference in the XRD patterns with or without Fe_2O_3. The only impact of the Fe_2O_3 addition is the dissolution of the exsolved Pd into Fe matrix at 800 °C. The complete Pd dissolution into surrounding Fe suggests that the Pd exsolution is a surface phenomenon. There is no evidence of sub-surface nucleation of Pd in lanthanum ferrite.

The Pd dissolution into A-site full lanthanum ferrite in the air gave rise to the emergence of Fe_2O_3. The incoming Pd released Fe out of the perovskite lattice. This iron oxide formation is, however, temperature-dependent. With high-temperature annealing in air, the Fe_2O_3 particles disappear. The lanthanum ferrite perovskite lattice incorporated residual Fe_2O_3 and PdO when heated to 1500 °C.

Acknowledgements

T.-S. Oh acknowledges the financial support from Auburn University. This work was also conducted under the framework of the research and development program of the Korea Institute of Energy Research (C2-2466). Some X-ray diffraction patterns were collected using a Rigaku SmartLab instrument purchased with support from the National Science Foundation Major Research Instrumentation program through grant NSF-DMR-2018794.

Data and code availability

Raw data will be available upon a direct request to the corresponding author.

Declarations

Conflict of interest None.

Ethical approval Not Applicable.

Supplementary Information: The online version contains supplementary material available at https://doi.org/10.1007/s10853-023-08346-1.

References

[1] Neagu D, Oh T-S, Miller DN, Ménard H, Bukhari SM, Gamble SR et al (2015) Nano-socketed nickel particles with enhanced coking resistance grown in situ by redox exsolution. Nat Commun 6:8120. https://doi.org/10.1038/ncomms9120

[2] Myung J, Neagu D, Miller DN, Irvine JTS (2016) Switching on electrocatalytic activity in solid oxide cells. Nature 537:528–531. https://doi.org/10.1038/nature19090

[3] Nishihata Y, Mizuki J, Akao T, Tanaka H, Uenishi M, Kimura M et al (2002) Self-regeneration of a Pd-perovskite catalyst for automotive emissions control. Nature 418:164–167. https://doi.org/10.1038/nature00893

[4] Zubenko D, Singh S, Rosen BA (2017) Exsolution of Re-alloy catalysts with enhanced stability for methane dry reforming. Appl Catal B 209:711–719. https://doi.org/10.1016/j.apcatb.2017.03.047

[5] Granger P, Renème Y, Lahougue A, Hamon C, Dhainaut F (2020) Thermal aging of perovskite based natural gas vehicle catalysts: dependency of the mode of Pd incorporation. Top

Catal 63:1474–1484. https://doi.org/10.1007/s11244-020-01331-x

[6] Eyssler A, Mandaliev P, Winkler A, Hug P, Safonova O, Figi R et al (2010) The effect of the state of Pd on methane combustion in Pd-doped $LaFeO_3$. J Phys Chem C 114:4584–4594. https://doi.org/10.1021/jp911052s

[7] Madsen BD, Kobsiriphat W, Wang Y, Marks LD, Barnett SA (2007) Nucleation of nanometer-scale electrocatalyst particles in solid oxide fuel cell anodes. J Power Sources 166:64–67. https://doi.org/10.1016/j.jpowsour.2006.12.080

[8] Bierschenk DM, Potter-Nelson E, Hoel C, Liao Y, Marks L, Poeppelmeier KR et al (2011) Pd-substituted (La, Sr)$CrO_{3-\delta}$–$Ce_{0.9}Gd_{0.1}O_{2-\delta}$ solid oxide fuel cell anodes exhibiting regenerative behavior. J Power Sources 196:3089–3094. https://doi.org/10.1016/j.jpowsour.2010.12.050

[9] Shin TH, Okamoto Y, Ida S, Ishihara T (2012) Self-recovery of Pd nanoparticles that were dispersed over La(Sr)Fe(Mn)O_3 for intelligent oxide anodes of solid-oxide fuel cells. Chem Eur J 18:11695–11702. https://doi.org/10.1002/chem.201200536

[10] Zhang J, Xie K, Zhang Y, Yang L, Wu G, Qin Q et al (2014) Composite titanate cathode decorated with heterogeneous electrocatalytic sites towards efficient carbon dioxide electrolysis. RSC Adv 4:22697–22709. https://doi.org/10.1039/C4RA02984D

[11] Adijanto L, Balaji Padmanabhan V, Küngas R, Gorte RJ, Vohs JM (2012) Transition metal-doped rare earth vanadates: a regenerable catalytic material for SOFC anodes. J Mater Chem 22:11396–11402. https://doi.org/10.1039/c2jm31774e

[12] Zhang W, Wang H, Guan K, Meng J, Wei Z, Liu X et al (2020) Enhanced anode performance and coking resistance by in situ exsolved multiple-twinned Co–Fe nanoparticles for solid oxide fuel cells. ACS Appl Mater Interfaces 12:461–473. https://doi.org/10.1021/acsami.9b14655

[13] Schmalzried H (1984) Oxide solid solutions and its internal reduction reactions. Ber Bunsenges Phys Chem 88:1186–1191. https://doi.org/10.1002/bbpc.198400046

[14] Ricoult DL, Schmalzried H (1987) Internal reduction of (Mg, Ni) O: effect of a NiO-concentration gradient. Phys Chem Miner 14:238–244. https://doi.org/10.1007/BF00307988

[15] Backhaus-Ricoult M, Carter CB (1987) Mechanism of the Internal Reduction of (Mg, Cu)O. J Am Ceram Soc 70:C-291–C−294. https://doi.org/10.1111/j.1151-2916.1987.tb04903.x

[16] Backhaus-Ricoult M, Ricoult D (1988) Electron microscopy of internally reduced (Mg, Ni)O. J Mater Sci 23:1309–1316. https://doi.org/10.1007/BF01154594

[17] Backhaus-Ricoult M, Hagege S, Peyrot A, Moreau P (1994) Internal reduction of chromium-doped alpha-alumina. J Am Ceram Soc 77:423–430. https://doi.org/10.1111/j.1151-2916.1994.tb07010.x

[18] Backhaus-Ricoult M (1998) Effect of volume changes during precipitation on internal reaction kinetics. Z Phys Chem 206:1–20. https://doi.org/10.1524/zpch.1998.206.Part_1_2.001

[19] Wagner C (1968) Internal oxidation of Cu-Pd and Cu-Pt alloys. Corros Sci 8:889–893. https://doi.org/10.1016/S0010-938X(68)80142-8

[20] Kwon O, Joo S, Choi S, Sengodan S, Kim G (2020) Review on exsolution and its driving forces in perovskites. J Phys Energy 2:032001. https://doi.org/10.1088/2515-7655/ab8c1f

[21] Joo S, Kwon O, Kim K, Kim S, Kim H, Shin J et al (2019) Cation-swapped homogeneous nanoparticles in perovskite oxides for high power density. Nat Commun 10:697. https://doi.org/10.1038/s41467-019-08624-0

[22] Eyssler A, Winkler A, Safonova O, Nachtegaal M, Matam SK, Hug P et al (2012) On the state of Pd in perovskite-type oxidation catalysts of composition A(B, Pd)$O_{3\pm\delta}$ (A = La, Y; B = Mn, Fe, Co). Chem Mater 24:1864–1875. https://doi.org/10.1021/cm300571y

[23] Oh T-S, Rahani EK, Neagu D, Irvine JTS, Shenoy VB, Gorte RJ et al (2015) Evidence and model for strain-driven release of metal nanocatalysts from perovskites during exsolution. J Phys Chem Lett 6:5106–5110. https://doi.org/10.1021/acs.jpclett.5b02292

[24] Uenishi M, Tanaka H, Taniguchi M, Tan I, Sakamoto Y, Matsunaga S et al (2005) The reducing capability of palladium segregated from perovskite-type $LaFePdO_x$ automotive catalysts. Appl Catal A 296:114–119. https://doi.org/10.1016/j.apcata.2005.08.031